



Adaptive optics via self-interference digital holography for non-scanning three-dimensional imaging in biological samples

TIANLONG MAN,^{1,2} YUHONG WAN,^{1,2,*} WUJUAN YAN,³ XIU-HONG WANG,³
ERWIN J. G. PETERMAN,^{4,5} AND DAYONG WANG^{1,2}

¹*Institute of Information Photonics Technology, Beijing University of Technology, 100 Ping Le Yuan, Chaoyang District, Beijing 100124, China*

²*College of Applied Sciences, Beijing University of Technology, 100 Ping Le Yuan, Chaoyang District, Beijing 100124, China*

³*Laboratory for Biomedical Photonics, Institute of Laser Engineering, Beijing University of Technology, Beijing 100124, China*

⁴*Department of Physics and Astronomy, Vrije Universiteit, Amsterdam, The Netherlands*

⁵*LaserLaB Amsterdam, Vrije Universiteit, Amsterdam, The Netherlands*

*yhongw@bjut.edu.cn

Abstract: Three-dimensional imaging in biological samples usually suffers from performance degradation caused by optical inhomogeneities. Here we proposed an approach to adaptive optics in fluorescence microscopy where the aberrations are measured by self-interference holographic recording and then corrected by a post-processing optimization procedure. In our approach, only one complex-value hologram is sufficient to measure and then correct the aberrations, which results in fast acquisition speed, lower exposure time, and the ability to image in three-dimensions without the need to scan the sample or any other element in the system. We show proof-of-principle experiments on a tissue phantom containing fluorescence particles. Furthermore, we present three-dimensional reconstructions of actin-labeled MCF7 breast cancer cells, showing improved resolution after the correction of aberrations. Both experiments demonstrate the validity of our method and show the great potential of non-scanning adaptive three-dimensional microscopy in imaging biological samples with improved resolution and signal-to-noise ratio.

© 2018 Optical Society of America under the terms of the [OSA Open Access Publishing Agreement](#)

OCIS codes: (090.1995) Digital holography; (180.6900) Three-dimensional microscopy; (110.1080) Active or adaptive optics; (110.1758) Computational imaging.

References and links

1. B. Rappaz, P. Marquet, E. Cuche, Y. Emery, C. Depeursinge, and P. Magistretti, "Measurement of the integral refractive index and dynamic cell morphometry of living cells with digital holographic microscopy," *Opt. Express* **13**(23), 9361–9373 (2005).
2. S. Przbilla, S. Dartmann, A. Vollmer, S. Ketelhut, B. Greve, G. von Bally, and B. Kemper, "Sensing dynamic cytoplasm refractive index changes of adherent cells with quantitative phase microscopy using incorporated microspheres as optical probes," *J. Biomed. Opt.* **17**(9), 0970011 (2012).
3. J. Rosen and G. Brooker, "Digital spatially incoherent Fresnel holography," *Opt. Lett.* **32**(8), 912–914 (2007).
4. B. Katz, J. Rosen, R. Kelner, and G. Brooker, "Enhanced resolution and throughput of Fresnel incoherent correlation holography (FINCH) using dual diffractive lenses on a spatial light modulator (SLM)," *Opt. Express* **20**(8), 9109–9121 (2012).
5. R. Kelner and J. Rosen, "Spatially incoherent single channel digital Fourier holography," *Opt. Lett.* **37**(17), 3723–3725 (2012).
6. A. Vijayakumar, Y. Kashter, R. Kelner, and J. Rosen, "Coded aperture correlation holography—a new type of incoherent digital holograms," *Opt. Express* **24**(11), 12430–12441 (2016).
7. A. Vijayakumar and J. Rosen, "Interferenceless coded aperture correlation holography—a new technique for recording incoherent digital holograms without two-wave interference," *Opt. Express* **25**(12), 13883–13896 (2017).
8. G. Brooker, N. Siegel, J. Rosen, N. Hashimoto, M. Kurihara, and A. Tanabe, "In-line FINCH super resolution digital holographic fluorescence microscopy using a high efficiency transmission liquid crystal GRIN lens," *Opt. Lett.* **38**(24), 5264–5267 (2013).

9. N. Siegel, V. Lupashin, B. Storrie, and G. Brooker, "High-magnification super-resolution FINCH microscopy using birefringent crystal lens interferometers," *Nat. Photonics* **10**(12), 802–808 (2016).
10. A. Vijayakumar and J. Rosen, "Spectrum and space resolved 4D imaging by coded aperture correlation holography (COACH) with diffractive objective lens," *Opt. Lett.* **42**(5), 947–950 (2017).
11. R. Kelner, B. Katz, and J. Rosen, "Optical sectioning using a digital Fresnel incoherent-holography-based confocal imaging system," *Optica* **1**(2), 70–74 (2014).
12. T. Man, Y. Wan, F. Wu, and D. Wang, "Self-interference compressive digital holography with improved axial resolution and signal-to-noise ratio," *Appl. Opt.* **56**(13), F91–F96 (2017).
13. J. Rosen and G. Brooker, "Non-scanning motionless fluorescence three-dimensional holographic microscopy," *Nat. Photonics* **2**(3), 190–195 (2008).
14. H. R. G. W. Verstraete, M. Heisler, M. J. Ju, D. Wahl, L. Blik, J. Kalkman, S. Bonora, Y. Jian, M. Verhaegen, and M. V. Sarunic, "Wavefront sensorless adaptive optics OCT with the DONE algorithm for in vivo human retinal imaging [Invited]," *Biomed. Opt. Express* **8**(4), 2261–2275 (2017).
15. D. Burke, B. Patton, F. Huang, J. Bewersdorf, and M. J. Booth, "Adaptive optics correction of specimen-induced aberrations in single-molecule switching microscopy," *Optica* **2**(2), 177–185 (2015).
16. T. J. Gould, D. Burke, J. Bewersdorf, and M. J. Booth, "Adaptive optics enables 3D STED microscopy in aberrating specimens," *Opt. Express* **20**(19), 20998–21009 (2012).
17. M. O. Lenz, H. G. Sinclair, A. Savell, J. H. Clegg, A. C. N. Brown, D. M. Davis, C. Dunsby, M. A. A. Neil, and P. M. W. French, "3-D stimulated emission depletion microscopy with programmable aberration correction," *J. Biophotonics* **7**(1-2), 29–36 (2014).
18. B. R. Patton, D. Burke, D. Oswald, T. J. Gould, J. Bewersdorf, and M. J. Booth, "Three-dimensional STED microscopy of aberrating tissue using dual adaptive optics," *Opt. Express* **24**(8), 8862–8876 (2016).
19. N. Ji, D. E. Milkie, and E. Betzig, "Adaptive optics via pupil segmentation for high-resolution imaging in biological tissues," *Nat. Methods* **7**(2), 141–147 (2010).
20. M. K. Kim, "Adaptive optics by incoherent digital holography," *Opt. Lett.* **37**(13), 2694–2696 (2012).
21. F. Merola, Á. Barroso, L. Miccio, P. Memmolo, M. Mugnano, P. Ferraro, and C. Denz, "Biolens behavior of RBCs under optically-induced mechanical stress," *Cytometry A* **91**(5), 527–533 (2017).
22. L. Miccio, P. Memmolo, F. Merola, P. A. Netti, and P. Ferraro, "Red blood cell as an adaptive optofluidic microlens," *Nat. Commun.* **6**(6502), 6502 (2015).
23. S. G. Adie, B. W. Graf, A. Ahmad, P. S. Carney, and S. A. Boppart, "Computational adaptive optics for broadband optical interferometric tomography of biological tissue," *Proc. Natl. Acad. Sci. U.S.A.* **109**(19), 7175–7180 (2012).
24. P. Pande, Y. Z. Liu, F. A. South, and S. A. Boppart, "Automated computational aberration correction method for broadband interferometric imaging techniques," *Opt. Lett.* **41**(14), 3324–3327 (2016).
25. J. Thauang, P. Knutsson, Z. Popovic, and M. Owner-Petersen, "Dual-conjugate adaptive optics for wide-field high-resolution retinal imaging," *Opt. Express* **17**(6), 4454–4467 (2009).

1. Introduction

Quantitative imaging of integral refractive index and thickness of living cells by digital holographic microscopy (DHM) has benefits the study of cellular dynamics [1,2]. While the applications of DHM are restricted to the coherent imaging system, on the other hand, over past several years digital holography of spatial incoherent fluorescent samples has emerged as an attractive scanning-free three-dimensional (3D) imaging technique. The development of Fresnel incoherent correlation holography (FINCH) [3–5] and other modalities such as COACH [6,7] have been employed for super-resolution imaging [8,9], multi-spectrum imaging [10], confocal imaging [11] and other imaging modalities [12]. FINCH provides a powerful tool in biological applications where 3D imaging or tracking of the fluorescent labeled particles or structures is required [9,13]. The quality of the images obtained with FINCH, in particular at larger imaging depth, is, however, limited by optical aberrations introduced by the optical system or the sample itself. Adaptive optics (AO) can be utilized to solve this problem by detecting and compensating the aberrations in a direct or indirect way. Traditional direct AO relies on a physical wavefront detection instrument, typically a Shack Hartmann wavefront sensor (SHWS). This approach has, however, its limitations since light originating from or scattered back from different sample depths may obscure the detection of aberrations [14]. Additionally, the precise alignment of the SHWS and the wavefront modulator is often a challenge in practice.

Recently, indirect sensor-less AO methods have been proposed and developed to overcome the limitations of SHWS [15–19]. In these methods, however, tens of pictures of the same scene are required to detect the aberrations, which can lead to long total exposure

time in cases where aberrations are substantial. This can be detrimental for applications to living cells or tissue that suffer from photo-bleaching and photo-toxicity. In special cases, such as holographic adaptive optics, fewer images are sufficient. In this method the convolution of a point-object-hologram and an extended-object-hologram is calculated to compensate the aberrations [20]. The applicability of this method is still limited because not all samples contain a point-like structure that can be used as guide star. Thanks to the high sensitivity of the interferometric imaging modality such as DHM, cell elasticity can be investigated by detail wavefront analysis [21] and further used for adaptive wavefront controlling [22]. In analogy to these interferometric wavefront analysis techniques, a guide-star-free computational adaptive optics (CAO) method has been demonstrated for OCT imaging [23,24]. CAO is, however, hard to implement in conventional fluorescence microscopy, since the phase of the optical aberrations is lost in the detection process.

In FINCH, the light originating from each fluorophore is split into two parts by a spatial light modulator (SLM). The spatially self-coherent two waves can interfere with each other on the camera. For a single fluorophore, the 3D positions as well as the phase aberrations in the optical path are inherently encoded in the recorded hologram. It is thus possible to correct the aberrations computationally without the need for a wavefront sensor and a wavefront modulator. In this article, we propose a FINCH-based 3D fluorescence microscope with guide-star-free anisotropic aberration correction, in which the blurred, complex-value images in FINCH are compensated and improved by a digital optimization procedure. In this procedure, an image quality metric is optimized by changing a 2D phase filter in the Fourier domain. We believe that this guide-star-free method is well fit to practical applications, for the following reasons. First, its operating speed is faster than other methods since only one complex-value hologram is required. Furthermore, the holographic recording and digital AO correction process are independent and therefore the holograms can be captured with a higher speed and then post-processed off-line. Consequently, our method reduces the total amount of light required to excite the sample, compared to other sensor-less AO methods.

Our article consists of four sections. After this introduction, we present in the next section the methodology and simulation results of our self-interference digital holography and computational aberration correction method. In the third section we will describe the optical setup and experimental results obtained with it to demonstrate its validity and resolution performance. We will also show proof-of-principle experiments on a tissue phantom containing sub-resolution fluorescent particles. As a demonstration of the applicability of our approach to biological samples, we show 3D AO images of actin-labeled MCF7 breast cancer cells. In the final section, we will discuss the advantages, limitations and potential applications of our method.

2. Methodology and simulations

2.1 Theoretical analysis

A schematic illustrating the principle of recording fluorescence self-interference digital holograms is presented in Fig. 1. It shows a single fluorophore, on-axis, that is excited (not shown) and emits fluorescence (green), which is collected by objective L. Part of this light is phase modulated by the SLM acting as a positive lens and the other part passes through the SLM unaltered. The two spatially self-coherent light beams interfere with each other in the recording plane and the resulting Fresnel-zone-plate-like (FZP-like) hologram is captured by the charge coupled device (CCD). An extended, fluorescently labeled sample can be assumed to be composed of a multitude of fluorophores and in this way the hologram of such a sample can be explained as the incoherent superposition of the FZP-like holograms generated by each fluorophore in the sample. 3D information of the sample can be retrieved by digital reconstruction of the holograms. Direct-current-bias in the hologram and twin image can be suppressed by capturing three, four or more images with different phase shifts introduced by the SLM [3,13].

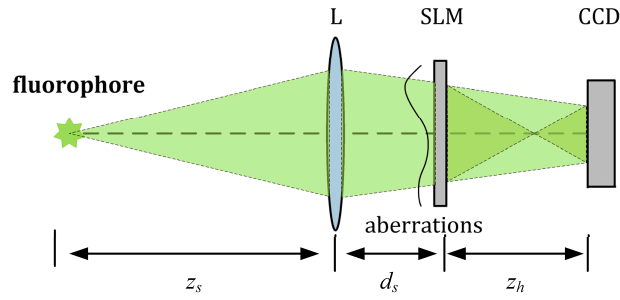


Fig. 1. Schematic of the fluorescence self-interference digital holography system used in the simulations.

The focal length of L is f . The distances from fluorophore to L, L to SLM and SLM to CCD are z_s , d_s and z_h respectively. The light field on the front surface of SLM, under the assumption that the emitted fluorescence is quasi-monochromatic, can be expressed as:

$$U_{\text{SLM}} = Q\left(\frac{1}{z_s}\right)Q\left(\frac{-1}{f}\right) * Q\left(\frac{1}{d_s}\right), \quad (1)$$

where $Q(1/a) = \exp[j\pi(x^2 + y^2)/(\lambda a)]$, λ is the central wavelength of the fluorescence, x and y are spatial coordinates, and $*$ is the two-dimensional convolution. Optical aberrations will deteriorate the performance of any imaging system, resulting in decreased resolution and signal-to-noise-ratio. System-introduced aberrations are typically caused by misalignment of the optical elements. Most sample-induced aberrations, on the other hand, are caused by inhomogeneities of the refractive index in the sample and mismatch between refractive index of the sample and immersion medium. To simulate such aberrations, we consider here, without loss of generality, an aberration in phase in the sample plane that is conjugate to the front surface of SLM. On the CCD plane the interference pattern has the form of I_i ,

$$I_i = \left| \begin{aligned} &Q\left(\frac{1}{z_s}\right)Q\left(\frac{-1}{f}\right) * Q\left(\frac{1}{d_s}\right)e^{j\varphi_a} * Q\left(\frac{1}{z_h}\right) \\ &+ Q\left(\frac{1}{z_s}\right)Q\left(\frac{-1}{f}\right) * Q\left(\frac{1}{d_s}\right)e^{j\varphi_a} Q\left(\frac{-1}{f_{\text{SLM}}}\right) * Q\left(\frac{1}{z_h}\right)e^{j\theta_i} \end{aligned} \right|^2 \quad (2)$$

where f_{SLM} is the focal length of the positive lens generated by the SLM, θ_i is the i -th phase-shift value and φ_a is the phase of the introduced optical aberrations. Zero-order terms (direct-current-bias) and the twin image in Eq. (2) can be eliminated using the phase-shifting technique. To this end, the complex-value hologram is calculated after recording four holograms with different θ value. Assuming unit magnification, the complex-value hologram of an extended fluorescence object can be expressed as

$$H_a = (E \cdot n) * H_p = (E \cdot n) * \left[Q\left(\frac{1}{z_r}\right) \cdot \Psi \right], \quad (3)$$

where E is the excitation intensity, n is the density distribution of fluorophores and z_r is the reconstruction distance. H_p is the aberrant complex-value hologram of a single fluorophore, which can be expressed as the product of the non-aberrant hologram $Q(1/z_r)$ and a phase aberration term Ψ that depends on φ_a . In conventional FINCH techniques, a reconstructed image of the object R_a can be obtained using the back-propagation algorithm, like:

$$R_a = H_a * Q\left(-\frac{1}{z_r}\right) = (E \cdot n) * \left[Q\left(\frac{1}{z_r}\right) \cdot \Psi \right] * Q\left(-\frac{1}{z_r}\right). \quad (4)$$

Equation (4) shows that the reconstructed image is blurred by the presence of aberration term Ψ . Different than in conventional fluorescence imaging systems, the phase of the aberrations is preserved in our self-interference holographic system. Therefore, the aberrations in Eq. (4) can be corrected by digitally applying a suitable phase mask φ_{AO} in the Fourier domain:

$$R_{AO} = \mathcal{F}^{-1}[\mathcal{F}(R_a) \cdot e^{j\varphi_{AO}}], \quad (5)$$

where \mathcal{F} and \mathcal{F}^{-1} denote the Fourier and inverse Fourier transforms. The phase mask can be expressed as a linear combination of the Zernike polynomials (z_m) up to k -th order with coefficients (c_m):

$$\varphi_{AO} = \sum_{m=1}^k c_m z_m. \quad (6)$$

Most guide-star-based sensor or sensor-less AO techniques detect and correct the aberrations in the pupil plane. In contrast, in our approach, the aberrations are compensated by applying a phase mask in the virtual pupil plane of the reconstructed image. Since FINCH provides 3D reconstruction ability, the system provides a series of virtual pupil planes that are arranged axially in the Fourier domain, each one corresponding to a reconstructed image at a certain depth in the sample. This is similar to multi-conjugate adaptive optics [25]. In our AO optimization process, the sharpness metric as defined in [16] can be used to evaluate the quality of the obtained reconstructions. The optimal coefficients $\hat{c} = [\hat{c}_1, \hat{c}_2, \dots, \hat{c}_m]^T$ for the Zernike modes applied to the phase mask that maximize the sharpness of the reconstructed image are obtained in a similar way as used for sensor-less AO [15,16]. In particular, the optimization is started from the lowest order Zernike polynomials. Orders are optimized one by one by generating several phase masks using random coefficients, measuring the AO corrected images and finding the optimal coefficients by Gaussian fitting of the coefficient-metric curve. Finally the optimal coefficients for all Zernike modes are used together to create the AO correction phase mask. The optimization procedure can be repeated to improve the quality of the corrected image.

2.2 Simulations

The validity and performance of the proposed method was first tested by simulations. The system shown in Fig. 1 was used and holograms of a 512×512 pixels USAF resolution test target were generated and reconstructed using both the conventional back-propagation algorithm and the proposed AO method. A central wavelength of $\lambda = 550$ nm was used and $z_s = 142.5$ mm, $d_s = 95$ mm, $f = 100$ mm, $z_h = 218$ mm, $f_{SLM} = 1200$ mm, respectively. Gaussian white noise was added to the generated holograms to simulate experimental noise.

To simulate an aberrated system, Zernike polynomials corresponding to astigmatism (z_3), coma (z_9) and spherical (z_{12}) aberrations were combined with coefficients $c_3 = 2$ rad, $c_9 = -4$ rad and $c_{12} = 2$ rad, respectively. The holograms were calculated and the conventional reconstructed image (Fig. 2(a)) was obtained using back-propagation algorithm. The corrected image, obtained using AO optimization with image sharpness as a metric, is presented in Fig. 2(b). Figure 2(b) shows that the image resolution and signal-to-noise ratio can be significantly improved by correcting the aberrations. The optimal retrieved coefficients by improving sharpness are $\hat{c}_3 = 1.8$ rad, $\hat{c}_9 = -1.6$ rad, and $\hat{c}_{12} = 1.4$ rad. It should be noted that these values are different than the original aberrations applied to the system, because of the inherent “self-reference” characteristics of self-interference holography: both of the signal and reference beams contain the object as well as the aberrations information. The recorded hologram is actually the difference between these two parts of information.

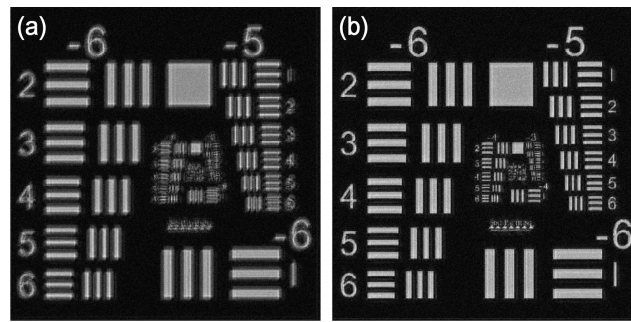


Fig. 2. (a) Simulated reconstructed image of USAF resolution test target using back-propagation algorithm with astigmatism (z_3), coma (z_9) and spherical aberrations (z_{12}) in the system. (b) AO corrected image obtained using the proposed method.

3. Experiments and discussions

3.1 Experimental setup

Experiments were performed on a custom-built FINCH inverted microscopic imaging system. The scheme of the system is shown in Fig. 3. The excitation laser source is a diode-pumped solid-state laser (85-BLT-605, Melles Griot) with central wavelength of 457 nm. The laser beam is reflected by two mirrors and coupled into a single-mode fiber (GCX-XSM-4/125-FC/PC-FC/PC, DHC) by a fiber coupler (PAFA-X-4-A, Thorlabs). The output light from the fiber is collimated and spectrally filtrated by a band-pass excitation filter F_{ex} (HQ470/40X, Olympus). The light is then reflected by a long-pass dichroic mirror DM (Q495lp, Olympus) and focused on the back focal plane of an infinity-corrected objective lens OBJ (TU Plan Fluor 20 \times /N. A. 0.45, Nikon) by an tube lens L_1 ($f_1 = 200$ mm AC254-200A, Thorlabs). The OBJ is placed on an inverted objective lens stage consisting of an objective lens holder (CSA1100, Thorlabs) and a vertical stage (M-MVN80, Newport). The sample is mounted on a sample stage consisting of an insert holder (MP100-MLSH, Thorlabs), a slide holder (MLS203P2, Thorlabs) and wide-field-illuminated by the excitation light. The emission from the specimen is collected by the OBJ and L_1 , transmitted by the DM, spectrally filtered by a long-pass emission filter F_{em} (HQ500lp, Olympus) and guided to the SLM (1024×768 pixels, $19 \mu\text{m}$ pixel pitch, LC-R2500, Holoeye) via an achromatic lens L_2 ($f_2 = 150$ mm AC254-150A, Thorlabs). The distance between L_1 and L_2 is 500 mm. A small angle of incidence (about 5°) on the SLM is used to avoid distortions. A cooled CCD camera (2048×2048 pixels, $7.4 \mu\text{m}$ pixel pitch, ML4022, FLI) is used to capture the image. The phase-modulation characteristics of the SLM were measured and user-defined by a look-up-table to ensure a linear phase modulation from 0 to 2π for light with a central wavelength of 550 nm. The wrapped phase map of a lens with focal length of $f_{SLM} = 1600$ mm is displayed on the SLM. Two polarizer P_1 and P_2 are used before and after the SLM in combination with polarization sensitivity of the SLM to achieve the wavefront division. The orientations of both polarizers are 45° with respect to the sensitive axis of the SLM. The CCD-SLM distance is chosen for maximum overlap of the two interference beams [8,12].

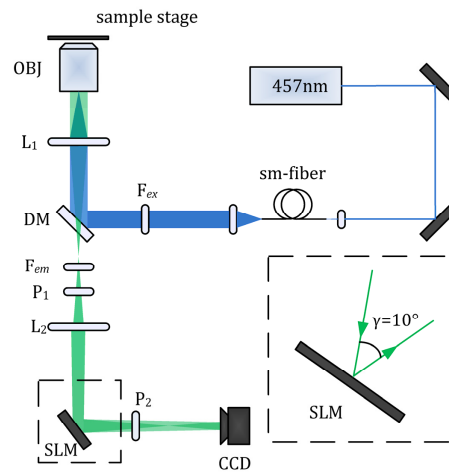


Fig. 3. Schematic drawing of the custom-built FINCH inverted microscopic imaging system. L_1 and L_2 , lens ($f_1 = 200$ mm, $f_2 = 150$ mm); DM, dichroic mirror; F_{ex} and F_{em} , filters; SLM, spatial light modulator; P_1 and P_2 , polarizers; OBJ, objective lens; sm-fiber, single mode fiber.

3.2 Aberration correction and resolution performance

The fluorescence specimen, consisting of a resolution test target (1951 USAF hi-resolution target, negative, Edmund Optics) and a fluorescent back-plate (365 nm excitation wavelength and 550 nm emission wavelength), was mounted in the focal plane of the objective. Optical aberrations were introduced by a specific Zernike-mode phase map on the SLM. This approach was taken in order to know the magnitude and type of the aberrations in the system, which makes quantitative evaluation of the performance of the AO methods possible. Astigmatism (z_3) with coefficient $c_3 = -20$ rad was first mapped on the SLM. Four phase-shifted holograms I_1 to I_4 ($\theta_1 = 0$, $\theta_2 = \pi/2$, $\theta_3 = \pi$ and $\theta_4 = 3\pi/2$) of the aberrant resolution target were recorded sequentially. A complex-value hologram H was calculated using $H = I_1 - I_3 - i(I_2 - I_4)$. The blurred sample image (Fig. 4(b)) was first reconstructed from H using back-propagation algorithm. Then in the AO correction process, starting with five randomly chosen c_3 values, the optimal coefficient was obtained by Gaussian fitting, resulting in $\hat{c}_3 = -6.28$ rad, Fig. 4(a). Finally, a phase mask was generated with this coefficient, and being applied to the reconstructed image (Fig. 4(c)). The diffraction limited resolving power of the system is $0.61/0.45 \times 550$ nm = 746 nm. Element 3 of group 9 (with a line width of 775 nm) of the resolution target can be clearly distinguished in the corrected image (Fig. 4(c)), while this same line pair is severely blurred and hard to resolve without AO correction (Fig. 4(b)). These sample images demonstrate that correcting the optical aberrations using the proposed method results in diffraction-limited images.

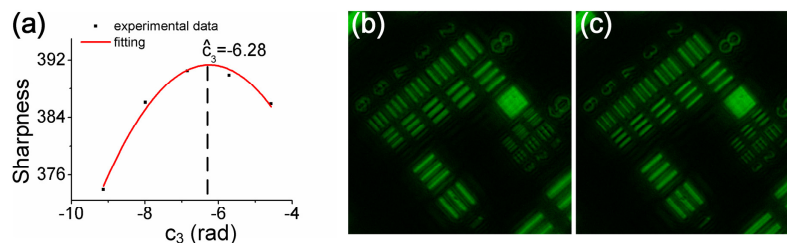


Fig. 4. (a) Schematic of AO optimization procedure of the experimental data with astigmatism (z_3) aberration in the system. Reconstructed image (b) before and (c) after the AO correction using the proposed method. Only the central area of the reconstructed images is shown.

To demonstrate the performance of the proposed AO method in a more complex aberrated system, astigmatism (z_3), coma (z_9) and spherical (z_{12}) aberrations with coefficients of $c_3 = -20$ rad, $c_9 = 20$ rad and $c_{12} = -4$ rad were applied to the system. For this experiment, we captured, in addition to the holograms, also regular wide-field images of the sample by using the SLM as an imaging lens. In this case, the unmodulated light was blocked by making the orientations of polarizers P_1 and P_2 collinear with the sensitive axis of the SLM. Wide-field images obtained in this way (Fig. 5(a) and 5(d)) were strongly deteriorated by aberrations, resulting in severe loss of resolution.

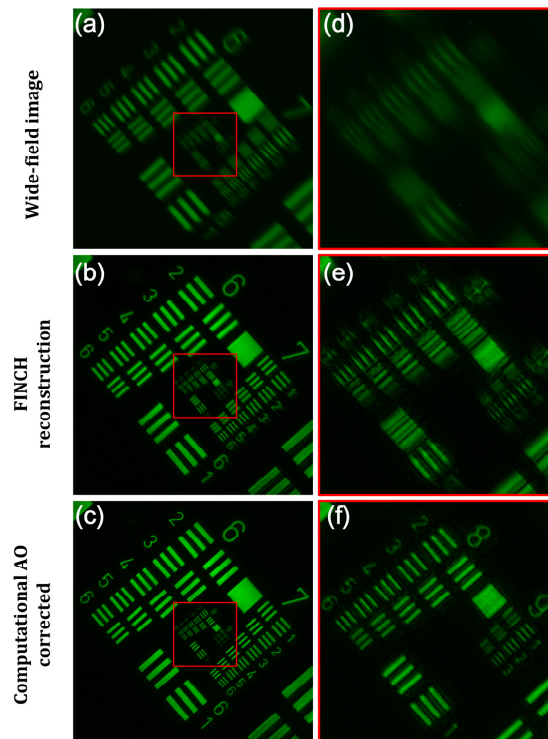


Fig. 5. Experimental results with astigmatism (z_3), coma (z_9) and spherical aberrations (z_{12}) in the system. (a) Aberrated wide-field image. (b) Conventional FINCH reconstructed image using back-propagation algorithm. (c) AO corrected image after using the proposed method. (d) - (f) Correspond to magnified image of the central area of (a)-(c).

The complex-value hologram was recorded. The reconstructed image was obtained from the complex-value hologram using the back-propagation algorithm and shown in Fig. 5(b) and 5(e). The image quality of these images is still not optimal. In particular, the resolution appears lower than the diffraction limit. Finally, the optimal coefficients of $\hat{c}_3 = -22.84$ rad, $\hat{c}_9 = -34.26$ rad, and $\hat{c}_{12} = 4.57$ rad for aberrations correction were obtained by applying our new AO correction method. A phase mask composed with these values was then applied to the reconstructed image, and a corrected image was calculated, shown in Fig. 5(c) and 5(f). These images obtained after aberration correction show remarkable improvements in sharpness, resolution and signal-to-noise-ratio.

3.3 Anisotropic aberrations correction of a tissue phantom

A 3D sample was made by embedding the 500nm fluorescent microspheres (yellow-green 505/515, Invitrogen) in 13.5% polyvinyl alcohol (PVA, $n = 1.52$) between the microscope slide and cover slip. The thickness of the sample was about $170\mu\text{m}$. Holograms of this sample

were captured using the setup shown in Fig. 3. After acquisition of four phase-shifted holograms, the complex-value hologram was extracted, the phase of which is shown in Fig. 6.

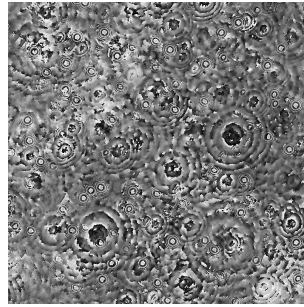


Fig. 6. Phase of the complex-value hologram of the microsphere sample.

In this phase map, multiple FZP-like holograms can be clearly discerned. Images were reconstructed using the back-propagation algorithm from the complex-value hologram with different propagation distances for refocusing, at depths of about $76\mu\text{m}$ (Fig. 7(a1)-7(a3)) and $120\mu\text{m}$ (Fig. 7(b1)-7(b3)) in the sample. Three microspheres located at different axial and lateral positions are indicated by arrows to demonstrate the digital refocusing ability of the system. Figure 7(a1) and 7(a3) show that microsphere 3 is in-focus at a depth of $76\mu\text{m}$, while microsphere 1 and 2 are out-of-focus. Figure 7(b1) and 7(b3) show the opposite: microsphere 1 and 2 are in-focus at a depth of $120\mu\text{m}$, while microsphere 3 is out-of-focus. It should be noted that, in fluorescence digital holography, in-focus images of microspheres located at different depths in the sample can be obtained from a single complex-value hologram. This is different from scanning microscopy, where multiple images with different focus depth need to be captured.

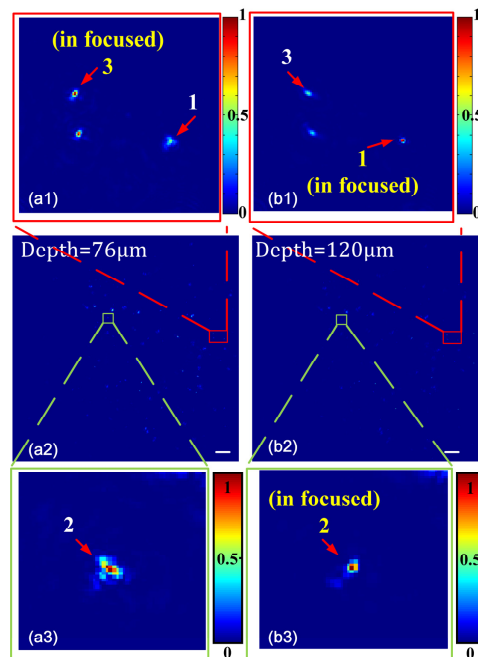


Fig. 7. Reconstructed images at (a1)-(a3) depths of $76\mu\text{m}$ and (b1)-(b3) $120\mu\text{m}$ in the sample. (a1), (b1) and (a3), (b3) are the magnified images of the areas labeled by red and green rectangles in (a2) and (b2). In (a1), (a3), (b1) and (b3), in-focus microspheres are indicated by the red arrows and yellow labels. The white scale bar indicates $10\mu\text{m}$.

The reconstructed images of the microspheres in Fig. 7 are substantially aberrated (e.g. microsphere 3 looks like an ellipse instead of an Airy disk) and show highly asymmetric out-of-focus diffraction patterns. In addition, optical aberrations induced by the sample depend on the spatial location of the microsphere: e.g. with increasing image depth, the reconstructed image of microsphere 2 (Fig. 7(b3)) appears more aberrated (the diffraction pattern looks more arcs-shaped) than that of microsphere 3 (Fig. 7(a1)). Furthermore, the images of microsphere 1 (Fig. 7(b1)) and 2 (Fig. 7(b3)) show that even at the same depth the aberrations can be different. To solve this problem, we segmented, before AO correction, the reconstructed complex-value image for a given reconstruction depth into multiple sub-region-of-interest (sROIs). Each sROI containing the in-focus image of one microsphere is chosen, thus the aberrations in each sROI are corrected individually. This procedure is repeated for all possible reconstruction depths. All of the 2D-corrected images obtained in this way are finally synthesized to generate a full-field-of-view 3D image with uniform diffraction-limited resolution. In this experiment, we used the summed square of pixel intensities as a metric for AO and used three sROIs at two reconstruction depths containing microsphere 1, 2 and 3 respectively. Four primary aberrations (defocus, astigmatism, coma and spherical aberrations, 3th to 9th and 12th orders of the Zernike polynomials) were corrected as shown in the bottom row of Fig. 8. To more clearly indicate the effects of optical aberrations on the image quality, we show the reconstructed image of each sROI without and with AO correction in Fig. 8.

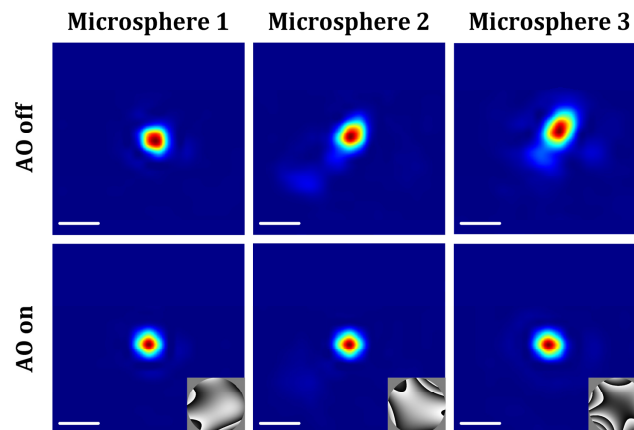


Fig. 8. Effect of aberration correction on reconstructed image of microsphere 1 and microsphere 2 (both located at a depth of $76\mu\text{m}$ in the sample) and microsphere 3 (located at $120\mu\text{m}$). Top row: reconstructed focal-plane images obtained using the back-propagation reconstruction method. Bottom row: reconstructed images with additional computational AO correction. Insets: phase masks used for the AO correction. Images are magnified 20 times using the image interpolation toolbox of the Matlab. The white scale bar indicates 880nm .

The uncorrected images in the top row of Fig. 8 demonstrate the presence of substantial, anisotropic sample-induced aberrations. For optimal correction of the images of microspheres, a different phase mask needs to be applied for each position in the sample (inset in Fig. 8). Using the proposed AO method, the quality of the AO corrected images (bottom row of Fig. 8) is substantially better than those obtained without AO. The aberrations (e.g. coma and spherical aberrations) appear very well compensated. These results demonstrate that with our new AO approach, 3D microscopy can be performed with improved resolution and image quality, uniformly over a large field-of-view. The aberration-corrected 3D reconstruction method is guide-star-free and can be obtained from a single complex-value hologram of the sample.

As an indication of the computational costs, on our state of the art desktop computer (Xeon E3-1230 3.3 GHz processor and 8 GB RAM), the average time required for correcting

seven primary (astigmatism, coma and spherical) aberrations in a 512×512 pixels complex-valued hologram was 167 s.

3.4 3D AO imaging of actin in MCF7 breast cancer cells

To demonstrate that our AO method can be applied to biological specimens, we imaged fluorescently labeled actin in fixed human cells. MCF7 breast cancer cells were grown on a 35mm polystyrene culture dish (35 mm TC-Treated Culture Dish, Corning). Cells were fixed in 4% paraformaldehyde and washed two times with PBS (Phosphate buffered saline). The F-actin in the cells was subsequently stained with ActinGreen 488 (ReadyProbes Reagent, Life Technologies). Coverslips (22×22 mm, 0.17 mm thickness) were washed twice with PBS and mounted on the culture dish using Prolong Diamond Antifade Mountant with DAPI (Life Technologies).

The optical system as shown in Fig. 3 was used to capture holograms of the cells. In this experiment, a sCMOS camera (2048×2048 pixels, 6.5 μm pixel pitch, ORCA-Flash 4.0 V3, Hamamatsu) was used to record the images with high sensitivity. The holograms of the sample were recorded, and the reconstructed images at two depths before and after AO correction are shown in Fig. 9. In [Visualization 1](#) a video is presented of an axial scan through the cell, showing reconstituted images every 0.25 μm in depth over a range of 10 μm .

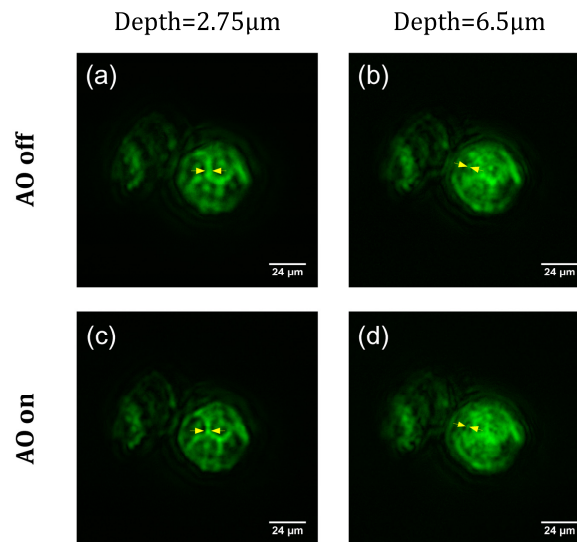


Fig. 9. Reconstructed images of actin-labeled MCF7 breast cancer cells (a)(b) before and (c)(d) after AO correction on different layers within the cell. Yellow arrows indicate the in-focus actin structures before/after AO correction. The scale bar indicates 24 μm (see [Visualization 1](#)).

The conventional reconstructed images from the hologram as shown in Fig. 9(a) are blurred by aberrations, for example induced by refractive index mismatch between the immersion medium of our objective (air) and the Antifade Mountant ($n = 1.47$). Using the proposed AO method with image sharpness as metric, coma and spherical aberrations are detected and corrected in the reconstructed image. The quality of the corrected image is improved as shown in Fig. 9(c). For example, the actin structure indicated by the yellow arrow is narrower in Fig. 9(c) than in Fig. 9(a). Despite the 3D imaging ability, reconstructed, AO corrected images of this sample are very similar to those obtained with the same system working under wide-field imaging mode (Fig. 10). Note that for 3D imaging using wide-field fluorescence microscopy, the sample needs to be scanned in the depth direction. Using our approach, images at different depth can be reconstituted from a single set of holograms

obtained without scanning the sample. This is demonstrated in Fig. 9(b) and 9(d) and [Visualization 1](#).

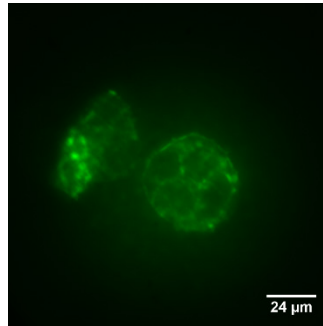


Fig. 10. Wide-field fluorescence image of the actin-labeled MCF7 breast cancer cells.

4. Conclusion

In this contribution, we have proposed and demonstrated a new kind of guide-star-free, sensor-less and modulator-free computational AO method for anisotropic aberration correction in fluorescence self-interference digital holography. We have presented a theoretical discussion of the recording and reconstruction procedure, demonstrating that the phase information of optical aberrations, which are completely lost in conventional fluorescence imaging, can be preserved in a self-interference digital holography system. Using this phase information, an AO optimization procedure that maximizes the sharpness or sum square of pixel intensity of the reconstructed image, can be implemented by computationally applying a suitable phase mask in the Fourier domain. The performance of our approach was first validated using simulations. To further demonstrate the potential of our approach, we performed experiments on a fluorescent resolution test target and a tissue phantom containing sub-resolution fluorescence particles. The results show significant improvements on image quality and signal-to-noise ratio after AO correction using our approach, compared to conventional wide-field imaging and conventional back-propagation algorithm reconstructions. The total exposure time of the sample is greatly reduced, since four exposures are sufficient to record a complex-value hologram that can be used to computationally compensate the optical aberrations. In addition, the anisotropic aberration correction of the proposed method enables 3D fluorescence imaging of thick samples, with uniform diffraction-limited lateral resolution over a large field-of-view. The relatively low sensitivity of the cooled CCD camera we used was a bottleneck for fast hologram acquisition. Furthermore, the calculations for the correction of anisotropic aberrations were relatively time consuming. The acquisition speed can be readily improved using a faster EMCCD or sCMOS camera. At the same time, the correction steps for each sROI are independent of each other and can be parallelized in a GPU. Our method can be readily implemented in any self-interference digital holographic system. Finally, the experimental results of actin-labeled MCF7 breast cancer cells demonstrate that our approach is compatible with biological samples and can be used to image subcellular structures in cells in 3D while correction for aberrations.

Funding

National Science Foundation (NSF) (61575009); Beijing Natural Science Foundation (4182016).

Acknowledgments

The authors would like to thank Prof. J. Rosen, Ben-Gurion University of the Negev, Beer-Sheva, Israel, for his discussion and feedback. We great acknowledge Prof. Tianrui Zhai and

Dr. Songtao Li, Beijing University of Technology, Beijing, China, for preparing the tissue phantom used in the experiment.

Disclosures

The authors declare that there are no conflicts of interest related to this article.